ARTICLE   OPEN

Check for updates

Oxidation kinetic behavior and microstructure mechanism of GH3536 alloy fabricated by laser powder bed fusion

S. L. Min[1,2,3], H. W. Zhang[1], H. Liu[1], L. H. He[1], S. Y. Qiu[1], F. Z. Chu[1], S. S. Huang[1], Y. Q. Wang[1], K. Zhang[1,4], J. J. Liang[3] and J. Hou [1]✉

This study comprehensively investigates the oxidation kinetics of laser powder bed fusion (LPBF) processed GH3536 superalloy at 950 °C. The oxidation kinetics and oxide film microstructure characteristics are analyzed and the underlying mechanism is discussed, by comparing with the conventionally manufactured wrought GH3536 samples under the exactly same test condition. The oxidation rate of LPBF samples is faster at initial stage and then tends to flatten out with increase of heating duration time. The finer and equiaxed chromia crystals formed in LPBF GH3536 surface can effectively improve the oxidation resistance comparing to the columnar structure chromia in wrought GH3536. The oxide film with excellent protection in LPBF GH3536 provides an important contribution to the application of GH3536 at high temperature.

npj Materials Degradation (2023)7:83 ; https://doi.org/10.1038/s41529-023-00399-6

INTRODUCTION

GH3536 (also known as Hastelloy X) is widely used in aviation engines and fuel nozzles for its exceptional high-temperature strength, toughness, and corrosion resistance[1–6]. The failure induced by high temperature oxidation in the air has a serious impact on the service life of such components as a long-term service product under high temperature conditions[7,8]. To date, the high temperature oxidation resistance of GH3536 has been taken into account of widely, several efforts are taken to comprehend the oxidation behavior[9–11]. Therein, oxidation kinetics act as an essential indicator to evaluate the various stages of oxidation and reflect the oxidation resistance of alloys. In the high temperature air atmosphere for long term exposure, GH3536 is reported to exhibit a parabolic oxidation kinetic; an outer layer of Mn-rich spinel accumulates on the grain boundaries and a continuously inner layer of Cr_2O_3 formed on the surface of matrix[12,13]. The compact and uniform inner film is of great significance for preventing the long-term high temperature oxidation and hot corrosion from aircraft turbine engine and prolonging the time life of GH3536 components.

Concerning the oxidation behavior of GH3536, the excellent oxidation resistance is related to the high Cr content (> 20%) in the alloy which could promote the formation of protective and continuous chromia oxide films when the alloy is exposed in high temperature harsh environment[11]. The Cr-rich inner layer leads to the rapid formation of the compact and protective oxide film, which acts as a barrier between the oxidizing atmosphere and the metal matrix, inhibits the inward and outward ions diffusing and sequentially impedes the subsequent oxidation[14]. As a primary factor impacting the oxidation resistance, the performance of oxide film under a certain temperature mainly depends on the layer structure, composition, compactness and stability. In the single crystal Ni-based superalloy, the hierarchical structure of oxide layer induces the multiple stages of oxidation kinetics[15]. The Ta-rich oxide formed on the inner layer causes the initiation of micro-voids and cracks and destroys the integrity of the inner layer due to the destructive effect of the tetragonal structure

Ta_2O_5 phase on the hexagonal structure Al_2O_3[15]. Internal stresses play an important role on the stability of oxide film, which generally reflect the spallation resistance of surface scale. The finer grain size and abundant defects in matrix could provide much more cores for nucleation of oxides, thus stress is released by facilitating creep deformation which leads to a significantly improvement of the oxidation resistance[16]. The microstructural characteristics of the oxide film in 304 L stainless steel is also systemically investigated while the oxide film from the outer to the inner layer consisted of faceted spinel particles, irregularly shaped hematite particles, and a compact layer of nano-sized spinel[17]. On the other hand, the surface morphologies and chemical compositions of oxide films also strongly impact the oxidation resistance of superalloy, the presence of Cr-oxide in the Co-based superalloy suppresses the formation of Co-oxide on the alloy surface due to the selective oxidation of Cr atoms[18]. In general, the characteristic of oxide film formed in the service process plays an important role to impede the degradation of alloys during high temperature oxidation.

Despite a large number of researchers spared no effort to improve the oxidation resistance by enhancing the protection of oxide films, the improvement of the anti-oxidation properties of such superalloys manufactured by conventional manufacturing methods is limited in high temperature. A reliable forming method is hence urgent to be developed. Meanwhile, owing to the difficulty of complicated structure and exorbitant processing costs, therefore, the concept of additive manufacturing is ultimately introduced to fabricate high-end and near-net-shape components. Laser powder bed fusion (LPBF) is one of the highly efficient additive manufacturing technologies that combined mental powder with high precision in a layer-by-layer manner allows for a greatly expanded design freedom with minimal feedstock waste. In addition to the superiority of flexible design and surface accuracy of components, several studies have reported that oxidation resistance could be greatly enhanced in a range of alloys through LPBF technology. The high quality LPBF GH3536 manufactured through optimized processing parameters is claimed to achieve excellent high temperature oxidation

[1]School of Materials Science and Chemistry, University of Shanghai for Science and Technology, Shanghai 200093, China. [2]School of Materials and Engineering, University of Science and Technology of China, Shenyang 110016, China. [3]Shi-changxu Innovation Center for Advanced Materials, Institute of Metal Research, Chinese Academy of Sciences, Shenyang 110016, China. [4]Monash Centre for Additive Manufacturing (MCAM), Monash University, Notting Hill, VIC 3168, Australia. ✉email: hou18217727686@163.com

resistance due to the ultrafine cellular structure and the nearly full dense products free of defects[19,20]. The ultrafine microstructure produced by the LPBF process slows down the overall oxidation rate through the formation of a more compact oxide scale without spallation in LPBF Nb-Si based alloy[21]. Similarly, the high-temperature oxidation resistance of pure chromium is great improved by controlling the crystallographic orientation during the LPBF process[22]. The enhancement of high-temperature oxidation resistance is also confirmed in Inconel 718 manufactured by LPBF technology that resulted from the refined and uniformly distributed microstructures during manufacture process[23]. Generally speaking, the ultrafine grain structures caused by rapid cooling and solidification during LPBF processing are of great significance for the enhanced oxidation resistance in a variety of alloys. As a crucial structure material in aerospace field, the LPBF technology of GH3536 has been well developed and successfully applied to the parts production. However, the researches on the high-temperature oxidation performance and the underlying mechanism on LPBF GH3536 are very limited, especially the role of oxide film on long-term hot corrosion and service reliability at the high temperature environment are not well understood. In addition, the microstructural characteristics of the oxide film formed on the LPBF GH3536 also lack systematic investigations and there is scope for more work to deeply study the oxide film.

The present work is aimed at investigating the oxidation kinetics and microstructural characteristics of the oxide film on LPBF GH3536 exposed in 950 °C dry air. Scanning electron microscopy (SEM), electron probe microanalysis (EPMA), TKD analysis and transmission electron microscopy (TEM) are applied to investigate the oxide film. The structure, element content, phase composition, oxide grain size, and compactness of oxide film are systematically studied in LPBF GH3536 and compared with the wrought GH3536. The related oxidation mechanism is discussed as well.

RESULTS

Microstructural features and isothermal oxidation kinetics

Figure 1 illustrates the metallurgical micrographs and original microstructures of GH3536 fabricated by wrought and LPBF before heat exposure. The macro-structure of LPBF sample along the horizontal plane exhibits molten pool with a droplet morphology where contains a large amount of ultrafine cellular sub-grains. By contrast, the wrought sample possess a coarser equiaxed grain morphology which contains carbides on the grain boundaries, as seen in Fig. 1b. The crystal orientation figure with grain boundaries of LPBF sample and wrought sample is also showed in Fig. 1c, d respectively. Compare to the random grain orientation in wrought sample, LPBF sample exhibits a stronger texture along the building direction.

Figure 2a shows the oxidation kinetics curves with error bars acquired through the weight gain distributions with the duration time for the isothermal oxidation at 950 °C in air for LPBF and
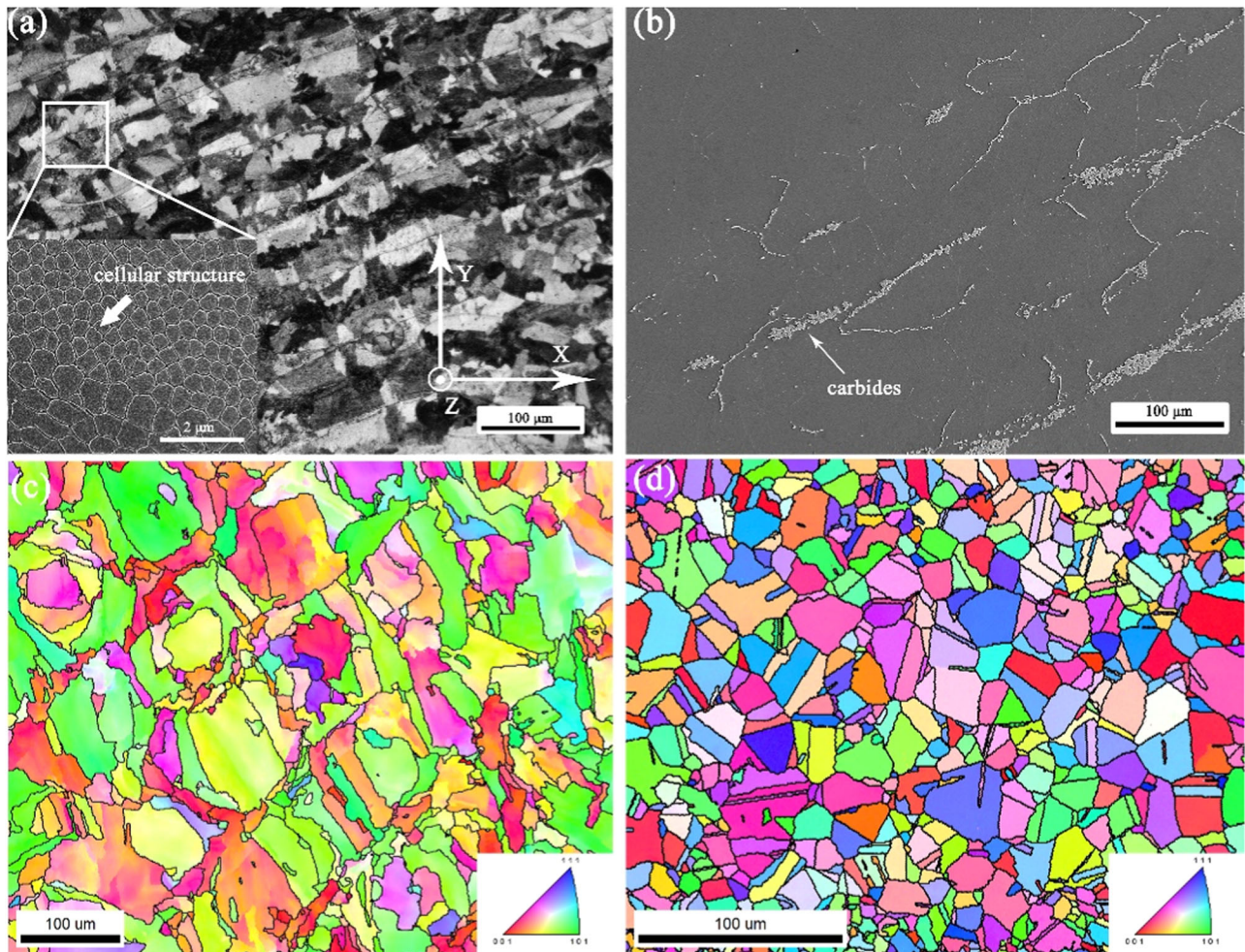

Fig. 1   Original microstructure of LPBF sample and wrought sample. a Optical and SEM images of the LPBF sample on the XOY plane. **b** SEM image of the wrought sample. **c** Inverse-pole figure of the LPBF sample. **d** Inverse-pole figure of the wrought sample.
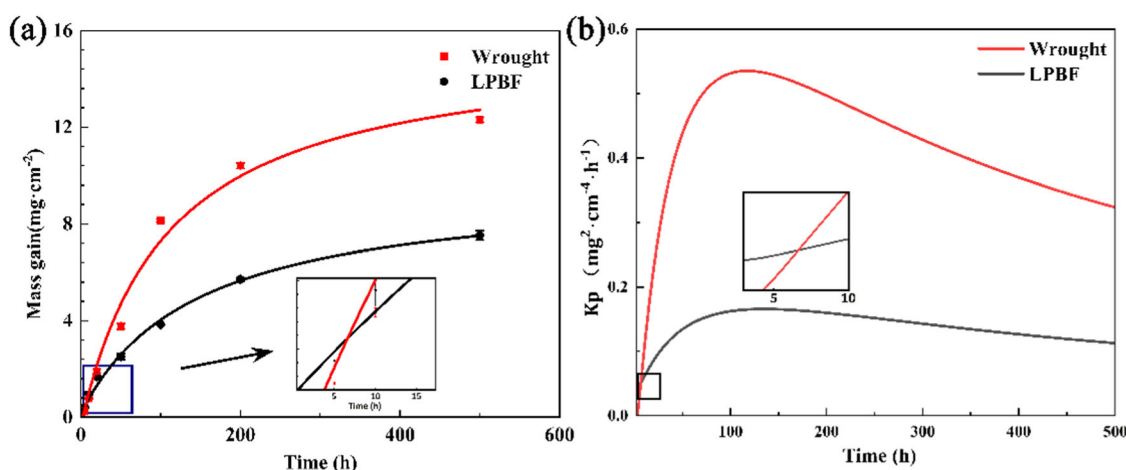
Fig. 2 High-temperature oxidation kinetics and oxidation rate constant of LPBF and wrought samples for 500 h. a Oxidation kinetics. **b** Oxidation rate constant.

wrought samples. For the long-term exposure up to 500 h, both the wrought and LPBF samples followed a classic parabolic time dependence of the weight gains after the transient oxidation period. With the variation of exposure time, the mass gain firstly displays a rapid increasing at the initial stage and keep stable gradually. Similarly, the oxidation rate constant fitted curve exhibits a same tendency with the results of mass gain, as seen in Fig. 2b. According to the Fig. 2a, the mass gain of wrought samples is slower than LPBF samples at the initial stage and surpass in turn with the duration time increased to 5 to 10 h, which is consistent well with the oxidation rate fitted curves. On the whole, higher mass gains are observed in the wrought samples after 500 h isothermal oxidation. That is, the LPBF GH3536 exhibits a better oxidation resistance than wrought samples after long-term high temperature oxidation which is consistent with previous work[20].

For having a deep understanding on the mass gain variation at the early stage of kinetics curves, four short-term oxidation samples of 1 h, 5 h, 10 h and 20 h exposure were selected for cross-section morphography, chemical composition and elements distribution measurement on the cross sections via SEM and EPMA (Fig. 3). From the SEM images and line scanning results of elements distribution on 1 h exposure samples, as seen in Fig. 3a, b, a thin Cr-rich layer of around 2.5 μm is formed on the surface of LPBF sample, while the wrought sample is slightly Cr enriched without the formation of oxide film. This result is consistent well with the above oxidation kinetics results that the mass gain of LPBF sample is higher at initial stage. In addition, an obvious Cr-depletion zone is observed underneath the outmost Cr enrichment layer on the LPBF samples after 1 h oxidation. With the increase of exposure time, a thick and compactness oxide film can be observed on both the LPBF samples and wrought samples with an increasingly apparent Cr-rich layer from 1 h to 20 h exposure. The oxide layers revealed marked differences in chemical composition among the LPBF and wrought samples. Therein, the oxide film in wrought samples is characterized by a hierarchical structure consisting of Mn-rich outer layer and Cr-rich inner layer while the LPBF samples feature a single Cr-rich layer oxide film (Fig. 3c, d). Significantly, the early-stage oxidation in LPBF sample features a thicker film than wrought samples up to 5 h exposing time whilst going into reverse with extended exposure. Figure 3e, f reveal a thinner oxide file and higher Cr enrichment in LPBF sample than wrought sample after exposed for 10 h. With the further extension to 20 h oxidation, the Cr-depletion zone under the scale is disappeared in the LPBF sample.

The phase component and surface morphology of oxide film
It is generally accepted that the initially formed oxide film acts as a barrier inhibiting the diffusion of O and alloy elements through scale. The performance and microstructure of oxide films are hence remarkable for the oxidation resistance of materials. Due to the significant difference between the structure and composition of oxide film, samples after exposure 20 h are selected for further analysis to investigate the microstructural characteristics of the oxide film. Both LPBF sample and wrought sample are sliding into a relatively steady stage in the weight gain curves and reasonable to form a protective film on the surface after 20 h high-temperature oxidation. The XRD and SEM are employed to analyze the structure and morphology of oxide films. Figure 4 shows the GI-XRD patterns of the oxide films formed on the surface of LPBF and wrought GH3536 after oxidation 20 h. The oxide film formed in LPBF samples is mainly consisted of a large amount Cr_2O_3 and small amount of $NiCr_2O_4$. On the contrast, the oxide film formed in wrought samples comprises large amounts of Cr_2O_3 and spinel ($MnCr_2O_4$ and $NiCr_2O_4$). The $MnCr_2O_4$ as the corrosion product is generated by selective oxidation of Mn in the matrix, which is corresponding to the Mn-rich outer layer in the cross-sectional line scanning result (Fig. 3h).

The surface morphology is characterized by SEM under high and low magnification, as shown in Fig. 5. Compared with the randomly distributed oxide particles formed on the surface of LPBF samples, the oxide particles formed on the surface of wrought samples tend to accumulate at the grain boundaries. According to the previous work[20], it can be confirmed that the Mn-rich outer layer is the main component of oxidation products on the grain boundaries in wrought samples. In LPBF GH3536, the morphology and oxides distribution are quite uniform and there is no obvious localized oxidized zone.

Oxide film cross section microstructure characteristics
To reveal the root causes for the oxidation performance differences between the LPBF and wrought samples, a series of precise characterizations are carried out on the cross-section samples of 20 h exposure. Figure 6 displays the cross-section morphologies and element distribution mappings via the EPMA mapping scanning analysis. The oxide film thickness of samples under two conditions is similar according to the cross-section images, which is well consistent with the results measured through line scanning of around 5.9 and 6.3 μm. But the elements distribution through the scale has significant differences: a uniform layer enriched with Cr and O without delamination is formed on LPBF sample whereas the wrought sample possesses a
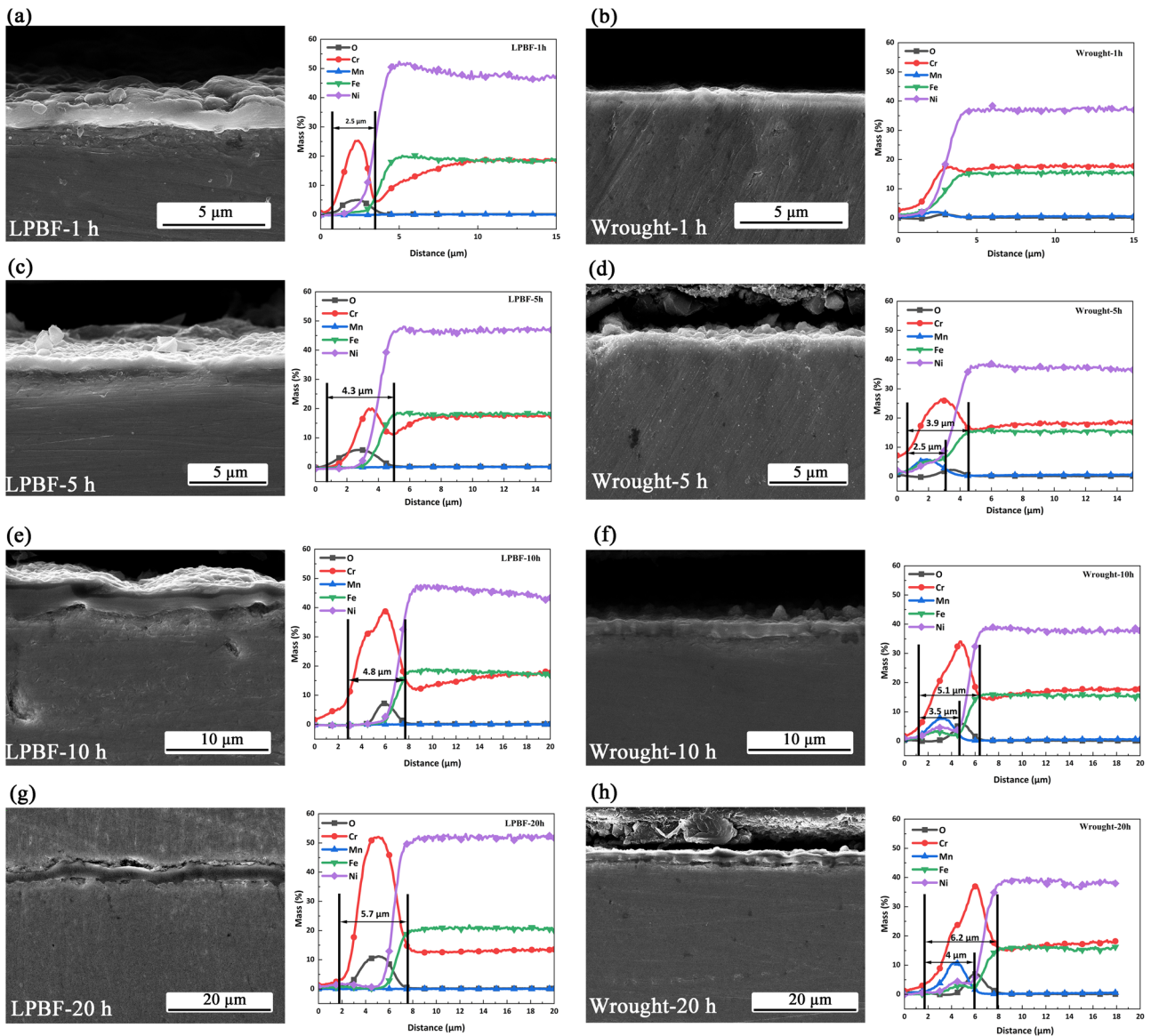
Fig. 3 The cross-section morphology and element distribution line analysis of LPBF and wrought samples after oxidation for 1 h to 20 h.
a LPBF sample after oxidation 1 h. **b** Wrought sample after oxidation 1 h. **c** LPBF sample after oxidation 5 h. **d** Wrought sample after oxidation 5 h. **e** LPBF sample after oxidation 10 h. **f** Wrought sample after oxidation 10 h. **g** LPBF sample after oxidation 20 h. **h** Wrought sample after oxidation 20 h.

duplex structure consisting of an outer Mn-rich layer and an inner Cr-rich layer The Mn-rich outer layer and Cr-rich inner layer respectively corresponds to the $MnCr_2O_4$ phase and Cr_2O_3 phase in the previous XRD patterns (Fig. 4). Moreover, a continuous Cr-depleted layer can be clearly observed below the inner layer.

Although the subtle differences of oxide film composition can be observed on the element distribution mappings, further characterization is required to explore the specific reasons for the diversity of oxide film formation between LPBF and wrought samples. TKD analysis was conducted to reveal the phase composition and cross-sectional topography of the entire oxide film in LPBF and wrought samples after 20 h oxidation, as shown in Fig. 7. Combined with the XRD pattern and phase analysis in Fig. 7a, e, the differences in structure of oxide films between LPBF sample and wrought sample are further determined. The oxide film in wrought sample is consisted of Cr_2O_3 phase and $MnCr_2O_4$ phase whereas the oxide film in LPBF sample is primarily composed of Cr_2O_3 single phase structure. Based on the inverse pole figures (IPF) with grain boundaries distribution throughout

the film on LPBF and wrought samples (Fig. 7b, f), the grain size gradient of Cr_2O_3 ranges from nanocrystalline at the near-matrix layer to coarse grained in the near-surface layer. Therefore, the observation of nanocrystalline at the near-matrix in two samples was conducted under high magnification to investigate the shape and size characteristics of Cr_2O_3 grains, as seen in Fig. 7c, g. Although the Cr_2O_3 grains exhibit a nanoscale feature in both LPBF and wrought samples, the grain size in former is much finer and the grain shape is near equiaxial in the nearest film-matrix interface whereas the grain shape in wrought sample is columnar. Figure 7d, h shows the pole figure and its intensity of Cr_2O_3 grains in Fig. 7a, e in LPBF and wrought samples.

The specific size and shape of the overall Cr_2O_3 grains in the oxide films of the LPBF and wrought samples were further evaluated through the statistics of grain characteristics in Fig. 7a, e. According to the grain size distribution chart in Fig. 8a, c, the number fraction of nanocrystals (grain size lower than 0.001 μm^2) in LPBF sample is much higher than that in wrought sample. These finer grains at the inner layer form a more compactness oxide film

in LPBF samples, which will inhibit the diffusion of elements in the oxide film and thus improves the oxidation resistance. As shown in Fig. 8b, d, the grain aspect ratio distribution chart of Cr_2O_3 grains reflects the shape of grains. When the aspect ratio is close to 1, the closer the grain shape is to equiaxed. There are more near equiaxed Cr_2O_3 grains (AR > 0.7) in the LPBF sample through the statistical results. Compared with the equiaxed grains, columnar grains provide wider channels for elements diffusion at early stage, which deteriorate the oxidation resistance of wrought sample.

The fine characterization of the oxide film structure and morphology is conducted using STEM on the LPBF and wrought cross-sectional samples fabricated by FIB, as shown in Fig. 9 and Fig. 10 respectively. The oxide film thickness obtained from the cross-sectional morphology by STEM observation matches well with the EPMA line scanning results. The selected area electron diffraction (SAED) patterns of the framed area marked as (1) and (2) in Fig. 9a indicate that both the outer surface and inner surface feature a rhombohedral structure and could be determined as Cr_2O_3 by EDS spot analysis in Table 1. Combining the SAED and EDS results on the framed area (3), it is confirmed a face centered cubic structure in the matrix. Figure 9c provides the high-resolution image acquired at the interface between oxide film and matrix. The oxides nucleate and grow outward into passive films along the outmost surface of matrix. The interface exhibits a coherent lattice matching at the interface. The result indicates that there is a coherent lattice interface between matrix and oxide film, and the metal substrate serves as propitious sites for nucleation of

oxides. Figure 9d shows the elements content profiles throughout the whole scale along the black line in Fig. 9a using EDS line scanning. The fluctuation of oxide film from outer layer to inner layer in element distribution is very small, which consists well with the single-layer structure of Cr_2O_3 film measured by EPMA. The TEM microstructure observation of wrought sample is shown in Fig. 10. The bilayer structure with inner and outer layer of oxide film is clearly visible. The framed areas of (1), (2) and (3) are selected for SAED analysis corresponding to the outer layer, inner layer and metal substrate, respectively, as shown in Fig. 10b1–b3. Different from the LPBF samples, the SAED pattern indicates that the grains of outer layer in the wrought samples possess a spinel structure. However, the SAED pattern of oxides in inner layer identify the same structure as that in LPBF samples. Moreover, the chemical composition distribution throughout the oxide scale to metal substrate is measured via EDS point scanning to determine the elements composition and verify the analysis of SAED patterns (Table 1). Compared to the LPBF sample, it is difficult to observed a clearly coherent relationship on the interface of wrought sample, as seen in Fig. 10c. Similarly, the EDS line analysis is conducted along the outer surface to the matrix, through the region 1, 2 and 3. The EDS profiles in Fig. 10d shows that the elements distribution in the oxide film of wrought samples fluctuates greatly compared with the LPBF samples. In the wrought samples, the oxide film is composed of the Mn-rich outer layer with the spinel structure and Cr-rich inner layer with rhombohedral structure, which is consistent with the previous result in TKD analysis.
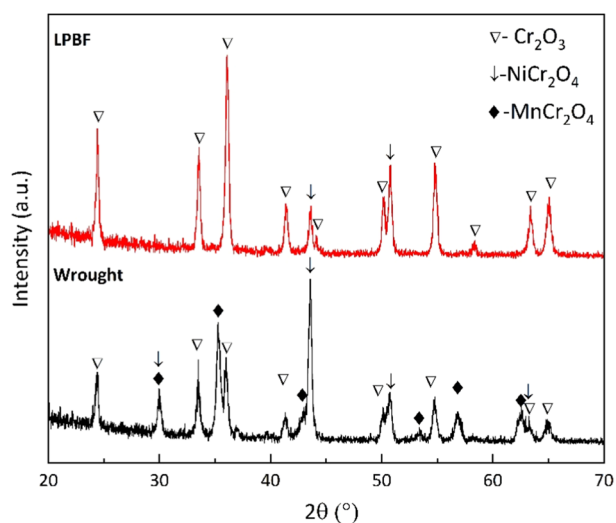
DISCUSSION

This work systematically investigated the oxidation behavior of LPBF processed GH3536 alloy by comparing with the conventionally wrought samples. The difference in oxide kinetics, surface morphology and oxidation species between LPBF and wrought samples will be discussed following.

The oxide kinetics curves with exposing time up to 500 hours are calculated from measured weight gain on LPBF and wrought samples. The major difference in kinetics curves is the obvious existence of a better oxidation resistance in LPBF under long-term high-temperature exposure, which has also been confirmed in related studies[20].

In order to further comprehend the oxidation mechanism of LPBF and wrought samples under the dynamic process, the oxidation behavior at different stages is discussed in combination with the oxidation kinetic results and the schematic diagram shown in Fig. 11. At the initial stage (< 1 h), the ultrafine microstructures (fine sub-grains with a mass of dislocations tangled on the grain boundaries) formed by extremely rapid solidification during manufacturing process accelerate the preferential formation of oxide film in LPBF GH3536. In contrast, the oxidation rate is slower at early stage in wrought GH3536 because
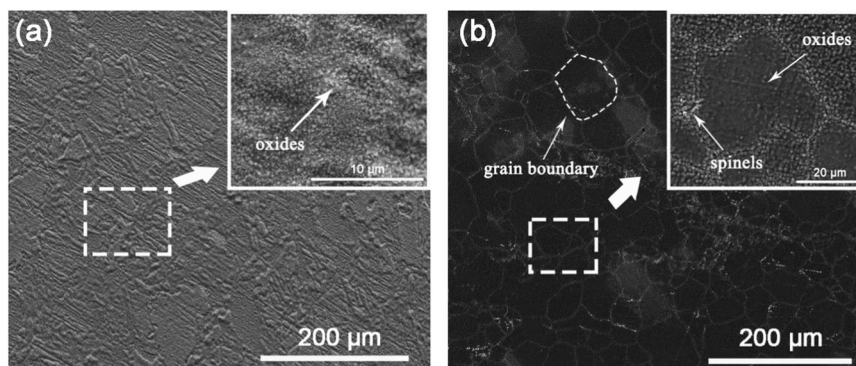

Fig. 4 XRD patterns of the oxide films formed on the LPBF and wrought samples after oxidation 20 h.

Fig. 5 Surface morphology of LPBF sample and wrought sample after oxidation 20 h. a LPBF sample. **b** Wrought sample.
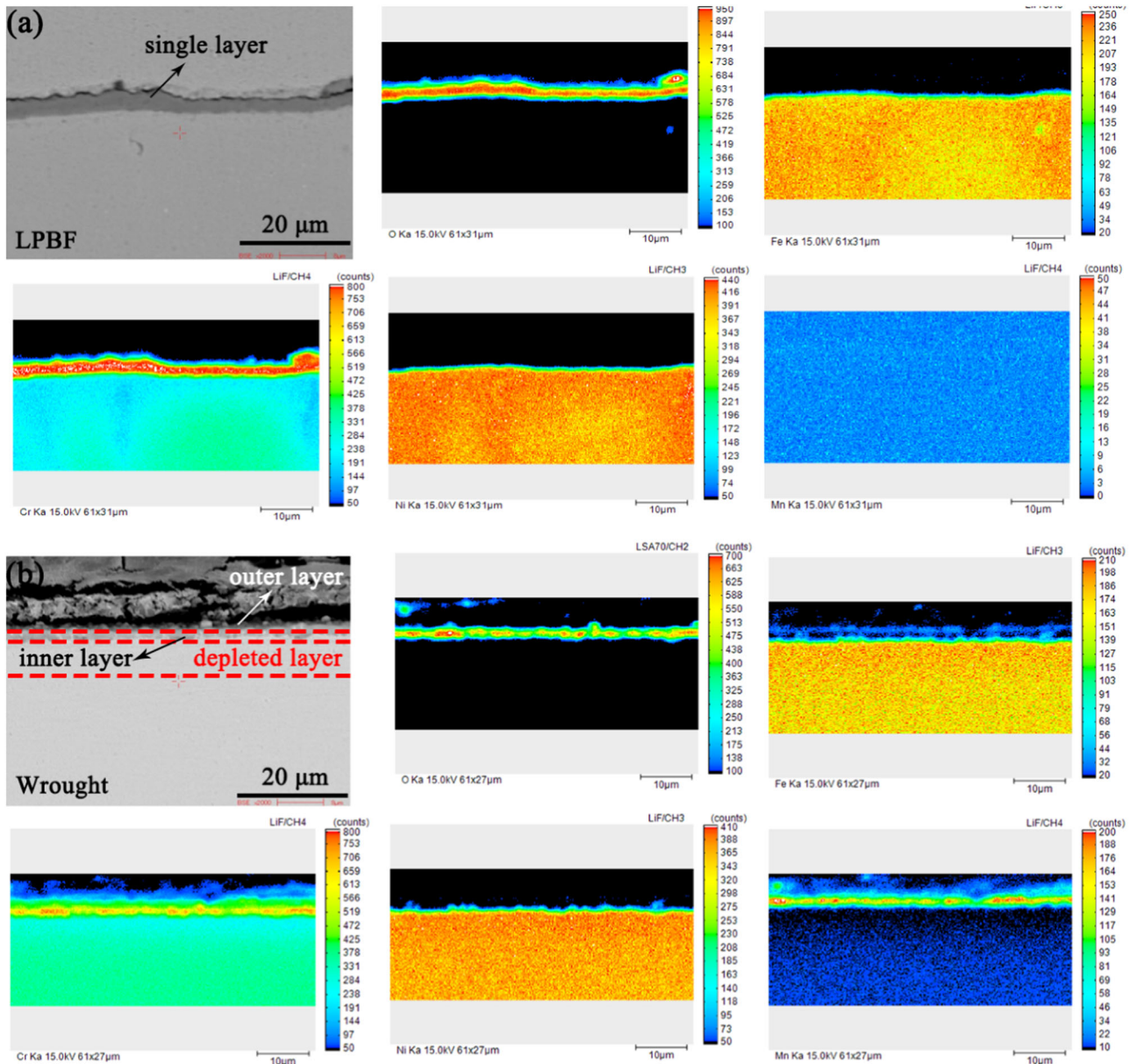
Fig. 6   Element distribution maps of LPBF samples and wrought samples after oxidation 20 h. a LPBF sample. **b** Wrought sample.

of the coarser grains structure leading to a lower diffusing rate controlled mainly by intragrain diffusion. As seen in Fig. 11a, b, a uniform single film is formed on the surface of LPBF sample while only a few oxide clusters formed on wrought sample. The kinetics at this stage confirms a higher mass gain in LPBF samples. With the increase of exposure time, oxidation proceeds to the next stage (1 h–20 h), as shown in Fig. 11c, d. At this stage, both LPBF samples and wrought samples form a compact oxide film and the oxidation rate gradually stabilizes. But it can be noticed that the composition and microstructure characteristics of oxide films in LPBF samples and wrought samples are different according to the above results. Herein, a consistent single layer Cr_2O_3 film covers LPBF sample surface whereas a duplex structure oxide film formed on the surface of wrought sample. As the oxide film in the LPBF sample forms preferentially in the previous stage, the decrease of oxidation rate is significantly faster that in wrought sample during this stage. With the extension of the exposure time, the oxidation kinetics curves for both samples intersect. Further extension of exposure time (> 20 h), oxidation enters the final stable stage like

Fig. 11e, f. At this time, the oxide film formed in LPBF sample developed the same composition as the wrought sample. However, the disparate structure and grain morphology (size and shape) in oxide film formed in previous stage determine the ability to impede diffusion at long-term high-temperature exposure. There is a large amount of spinel accumulates at grain boundaries due to the fast diffusion rate along the grain boundaries and the wide diffusion path provided by columnar grain in oxide film of wrought sample, which decreases the flatness and compactness of the oxide film. The consistent structure and equiaxed grains in oxide film of LPBF samples act as a more thorough barrier to inhibit diffusion. In summary, both Cr_2O_3 layer and spinel layer in LPBF sample is thinner than that in wrought sample. The oxidation kinetics at this stage shows that the mass gain of LPBF sample is lower and the oxidation rate is slower.

According to the above oxidation kinetics study, the oxidation rate significantly slows down when a compact film formed on the out surface. During the whole process, oxide film plays a crucial
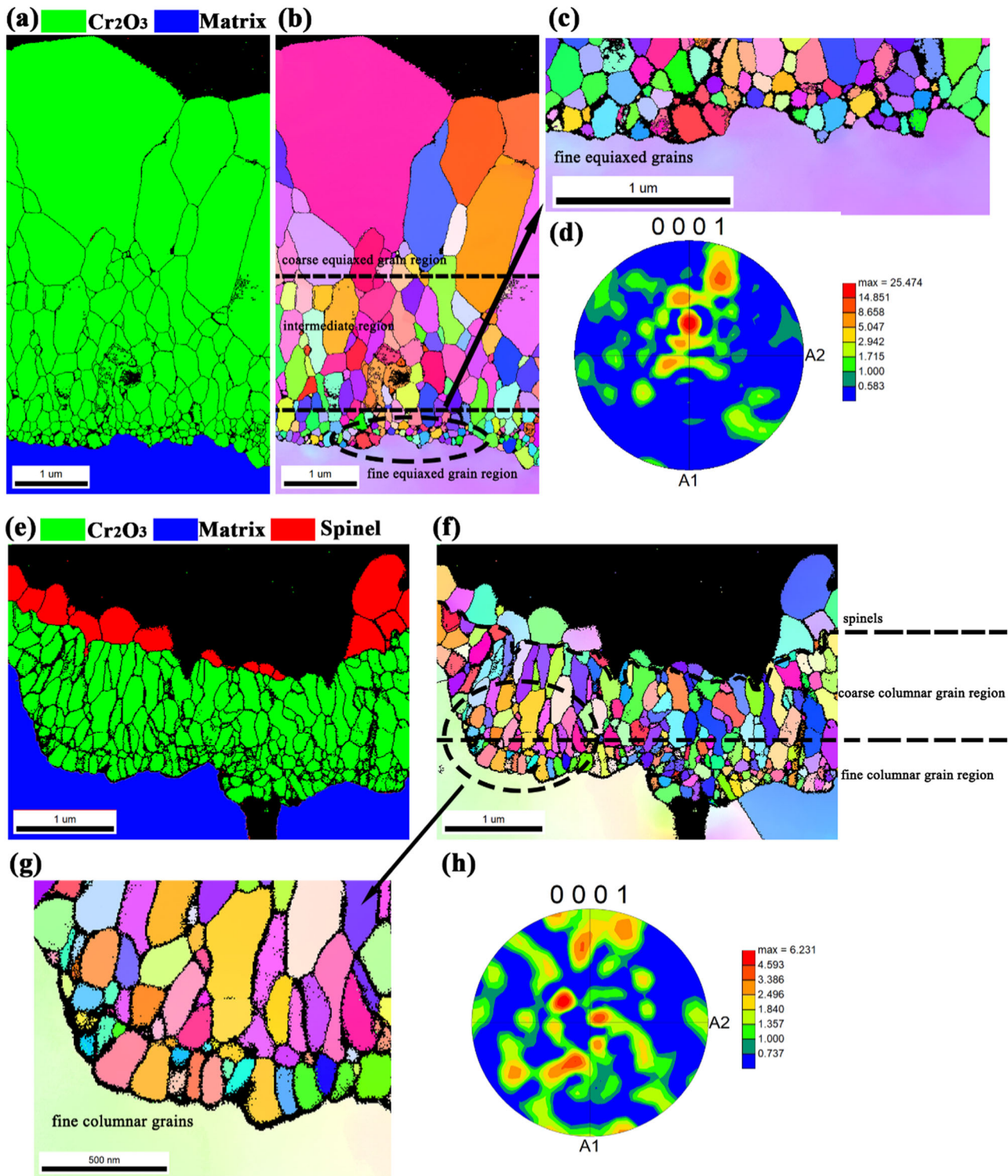
Fig. 7 TKD analysis of LPBF sample and wrought sample after oxidation 20 h. a Phase analysis of the LPBF sample. **b** Inverse pole figure of the LPBF sample. **c** Inverse pole figure of LPBF sample near the interface of matrix and oxide film. **d** Pole figure with intensity of LPBF sample. **e** Phase analysis of the wrought sample. **f** Inverse pole figure of the wrought sample. **g** Inverse pole figure of wrought sample near the interface of matrix and oxide film. **h** Pole figure with intensity of wrought sample.

role, thus the microstructure and stability of oxide film in the early stage have also been considered as the key to determine the overall oxidation performance for metals.

Although the oxide film is formed in both wrought samples and LPBF samples after 20 h exposure, the phase composition of the oxide film is significant different through the XRD analysis and TKD analysis (Figs. 4, 7). This depends on the chemical composition and the elements diffusion of the matrix. Herein, the elemental composition of matrix is close for two samples, which leading to a similar oxidation process that conforms
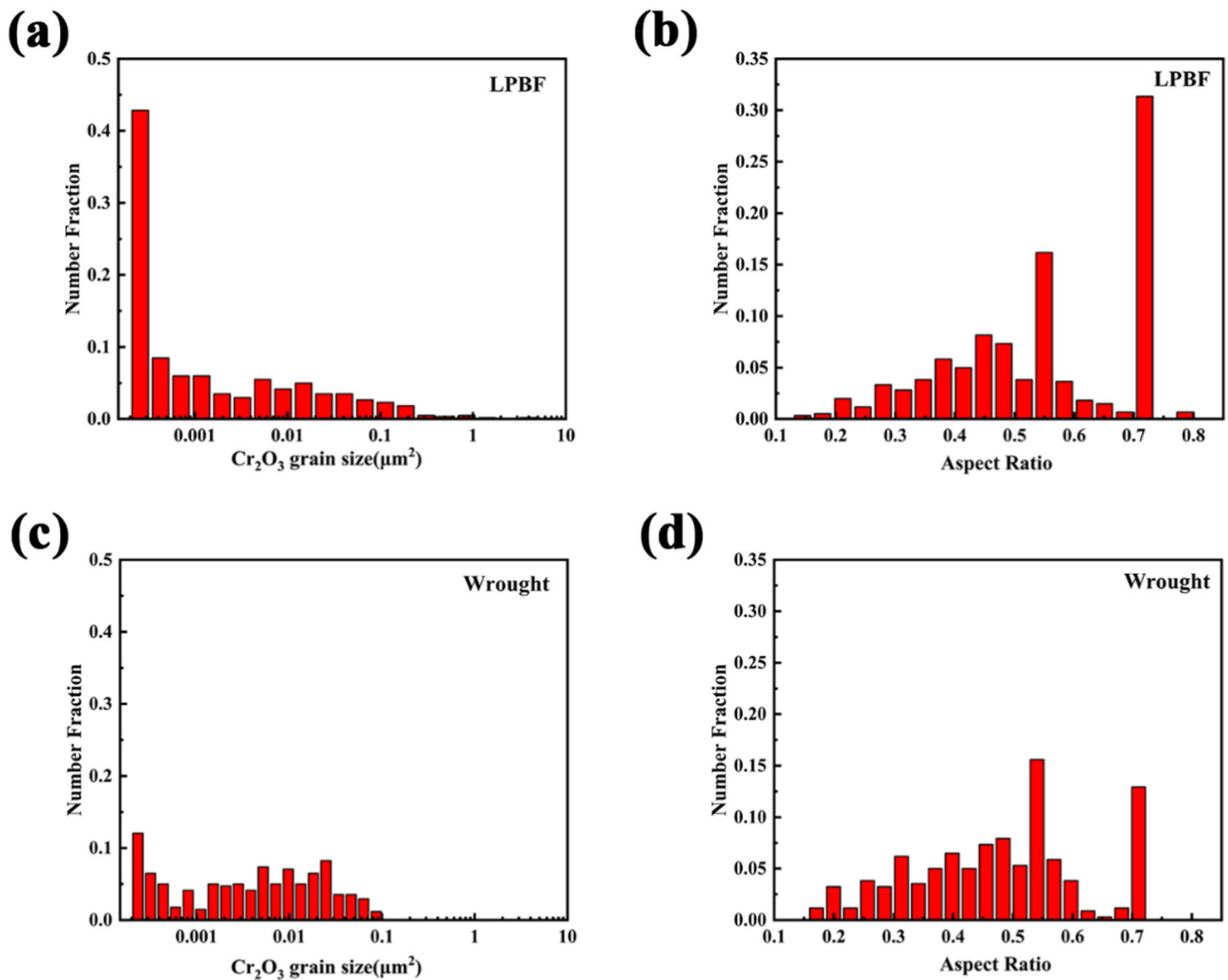
Fig. 8 Grain size distribution chart and grain aspect ratio distribution chart of LPBF and wrought sapmle. a Grain size of LPBF sample. **b** Grain aspect ratio of LPBF sample. **c** Grain size of wrought sample. **d** Grain aspect ratio of wrought sample.

parabolic law. Therefore, the diffusion of elements is dominant for the differences in phase composition and structure of oxide film. For GH3536 alloy prepared by conventional method, it is generally believed that the oxide film is composed of spinel outer layer and chromium oxide inner layer[13]. In the wrought samples, the accumulation of spinel on the outer layer is mainly led by the Cr depletion at the grain boundary caused by element segregation. When the concentration of Cr is lower than the critical concentration, the alloy element will further react with the oxide to form spinel. In the present study, the oxide film in LPBF samples is consisted of single chromium oxide. Combined with the EMPA analysis in Fig. 6, the faster diffusion rate in LPBF sample promotes oxidation reaction and continuously generates a dense Cr_2O_3 at the very early oxidation stage[24]. On the other hand, the content of Mn in LPBF sample is a little lower than that in wrought sample, which is another reason results the single layer structure in oxide film after 20 h oxidation[25].

Although the Mn content in LPBF samples and wrought samples is different, it has reported that the addition of 1% Mn has little effect on oxidation rate in Ni-20Cr alloys according to[26]. At present alloy system, the Mn content in both LPBF sample and wrought sample is lower than 1%. Due to the higher diffusion rate of Mn than Cr both in the lattice and at the grain boundary, which forms a thick spinels layer composed of $MnCr_2O_4$. Indeed, the

difference of oxide film structure will impact the oxidation resistance. However, the Cr_2O_3 layer as the key role in preventing oxidation, its microstructure characteristics dominates the oxidation behavior and oxidation process. In LPBF samples, the ultrafine matrix microstructure promotes the formation of the equiaxed and fine Cr_2O_3 grains, whereas the Cr_2O_3 grains formed in wrought samples are coarse and column. Meanwhile, the differences of microstructure in Cr_2O_3 layer also have impact on the formation of spinels layer, the spinels layer is also formed on the Cr_2O_3 layer after 500 h exposure according to our previous work[20] and current results. The hysteresis of the spinels layer formation in LPBF sample is largely attribute to the microstructure of matrix and Cr_2O_3 layer.

It is well-known that the Cr_2O_3 layer has better oxidation resistance than spinel layer[27]. The single layer structure of oxide film in LPBF sample undoubtedly shows a better performance. As the driving force of diffusion, the higher concentration gradient of Cr in the oxide film of LPBF samples can also effectively weaken the diffusion of alloy element from matrix outward to surface. Meanwhile, the thicker and denser Cr_2O_3 film in LPBF samples also significantly restrict the inward diffusion of O element. From this stage, the oxidation rate of LPBF sample is obviously slower than wrought sample. Therefore, the GH3536 produced by LPBF
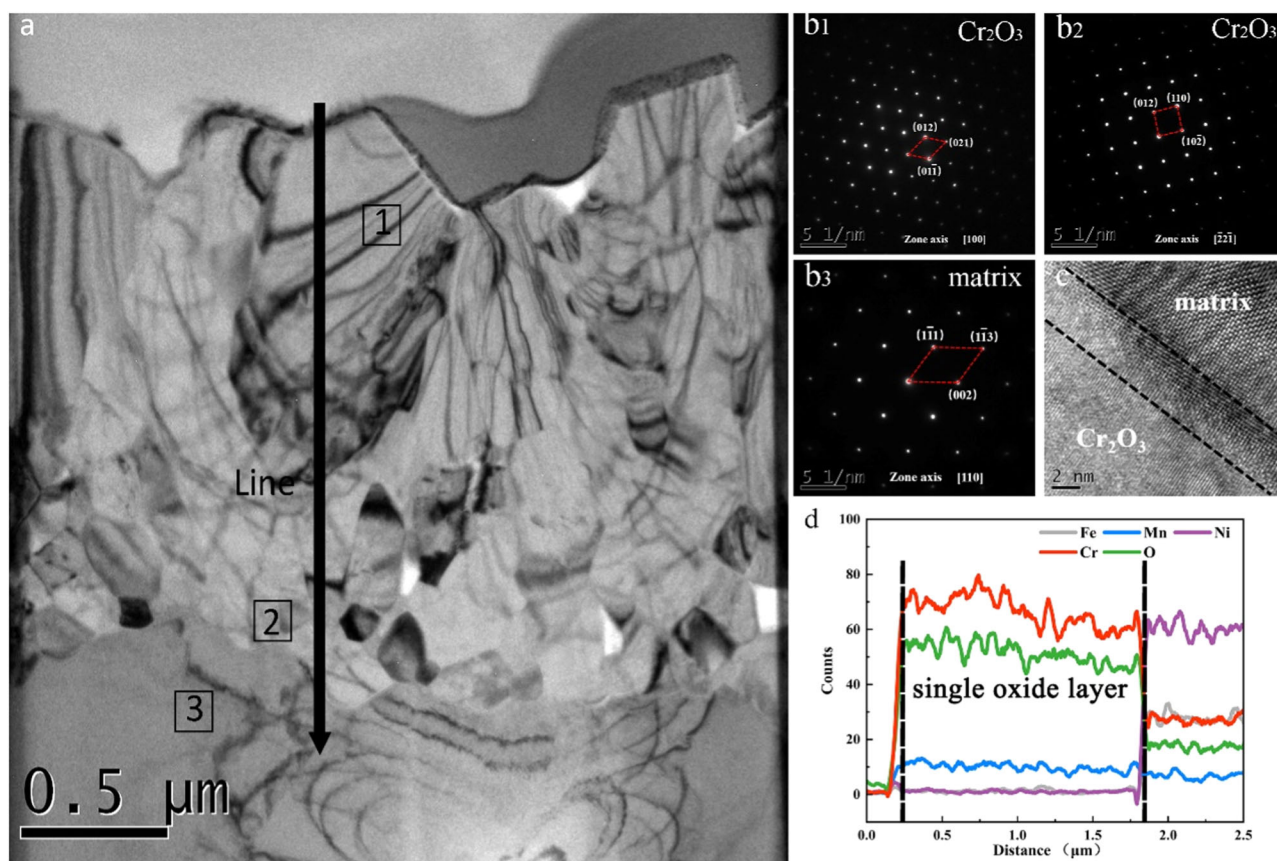
Fig. 9 TEM analysis of the LPBF sample after oxidation at 950 °C for 20 h. a Cross-sectional morphology. **b** SAED patterns of the framed area in **a**. **c** Hhigh-resolution image of the interface. **d** EDS line scanning result of black line in **a**.

exhibits a better oxidation resistance than wrought GH3536 under long-term service environment.

Based on the grain morphology statistics results by TKD, the Cr_2O_3 grains in the LPBF sample oxide film have a smaller average size and larger grain aspect ratio. At the initial stage, when the surface of samples is in contact with air and reaching the critical nucleation condition of Cr_2O_3, grains will continuously nucleate and grow. It has been reported in our previous work that the Cr element tend to segregate inside or along the sub-grain boundaries[19,20]. Although the local segregation of Cr element will lead to the inhomogeneous oxidation in wrought samples, it is different from the LPBF samples with ultrafine microstructure. On the contrary, the Cr element segregation on the sub-grain boundary provides more nucleation sites, which to a certain extent homogenizes the distribution of oxides. These large number of nucleation sites generate the Cr_2O_3 grains with smaller size and denser at the interface between the oxide film and the matrix. This also explains why the LPBF sample has a faster oxidation rate at the initial stage of oxidation. The grains usually are equiaxed after nucleation, while the grains will grow along the surface epitaxy during the growing process. Due to the fewer nucleation sites in the wrought sample, the Cr_2O_3 grains have sufficient time and space to grow and finally transition from equiaxed to columnar. In the LPBF samples, there are more Cr_2O_3 grains nucleate at the same time, which limits the growth of grains. Although the grains also grow outward along the direction perpendicular to the surface, the existence of cellular structure with a large number of dislocations tangling on the boundary lead to a much faster diffusion rate. The Cr_2O_3 grains lack enough time for growth before new grains rapidly begin to nucleate and eventually initial Cr_2O_3 grains retain the equiaxed shape. In

addition, when the compact oxide film is formed, the nucleation of Cr_2O_3 is difficult to maintain as diffusion becomes slower and the existing fine grains grow along the epitaxial direction continuous and eventually evolving into coarse grains in outer layer.

As for Cr_2O_3 film coating, it is generally believed that equiaxed structure grains possess a better corrosion resistance and large efforts have been made to prepare equiaxed structure coating in the past[28,29]. In this study, the GH3536 manufactured by LPBF can naturally generate Cr_2O_3 grains with well equiaxed morphology under high-temperature air environment. These fine equiaxed grains in the oxide film make the diffusion channel much more crowded and complicate, which can better inhibit further oxidation. Compared with the LPBF samples, the Cr_2O_3 film with columnar structure provides a broader and more convenient channel for the diffusion of O element. Besides, the oxidation resistance of spinel outer layer is worse. With the extension of oxidation time, wrought GH3536 will experience severe oxidation degradation than LPBF GH3536. Figure 12 is the schematic diagrams of diffusion of O element in oxide film with different grain morphography. The O element has a faster diffusion rate and the shorter diffusion path along the columnar grain boundary. Beyond the ability to impede the diffusion, the stability of oxide film also needs to be considered. According to the[16,30], the resistance to cracking is closely associated with the grain size. In the results of grain size statistics in Fig. 8, the average size of Cr_2O_3 grains in LPBF sample is lower than wrought, which means that the oxide film in LPBF samples can withstand greater thermal stress and growth stress during oxidation process.

In this study, the oxidation kinetics and oxide film microstructure characteristics at the early stage of GH3536 prepared by
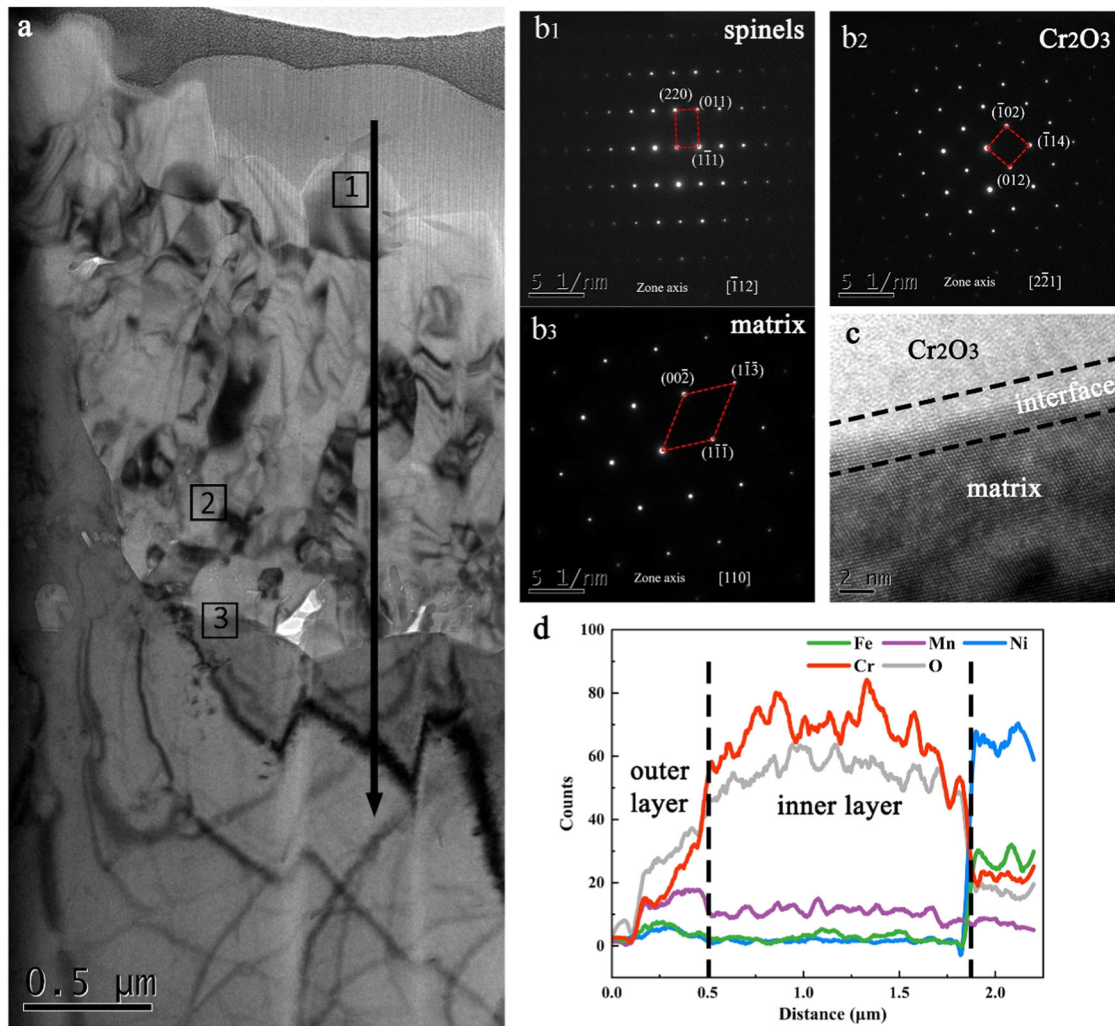
Fig. 10 TEM analysis of the wrought sample after oxidation at 950 °C for 20 h. a Cross-sectional morphology. **b** SAED patterns of the framed area in **a**. **c** High-resolution image of the interface. **d** EDS line scanning result of black line in **a**.

Table 1.   EDS analysis of the LPBF sample and wrought sample.

		O		Cr		Fe		Ni		Mn	
		wt.%	At.%	wt.%	At.%	wt.%	At.%	wt.%	At.%	wt.%	At.%
LPBF	a	31.58	60.16	61.13	35.82	\	\	0.71	0.36	6.56	3.64
	b	32.55	61.09	66.54	38.42	0.54	0.29	0.35	0.18	\	\
	c	1.94	6.54	19.63	20.36	19.91	19.22	56.63	52.02	1.87	1.83
Wrought	a	32.99	62.03	44.99	26.02	0.86	0.46	2.91	1.49	18.22	9.97
	b	39.46	67.97	59.28	31.41	0.94	0.46	0.30	0.14	\	\
	c	2.68	9.37	17.73	19.05	20.55	20.55	45.12	42.93	\	\

LPBF and wrought is systematically investigated. The microstructure difference of oxide film and its underlying formation mechanism are clearly clarified. The main conclusions can be drawn following:

1. The better oxidation resistance of LPBF processed GH3536 under long-term high-temperature exposure is resulted by the matrix microstructure. The oxidation rate is fast at the initial stage while it is much slower than wrought samples at stable stage.

2. The oxide film at early stage of LPBF GH3536 samples only contains the single chromia layer whereas there is a double-layer structure with an outer layer spinel in the oxide film of wrought samples.

3. A better oxidation resistance and long-term exposure stability of LPBF samples is majorly contributed to the finer-size chromia grains and equiaxed structure at the initial oxide film. The slower diffusion rate and more complicate diffusion path in equiaxed structure oxide film extend the service life of the GH3536 alloy at high temperature.
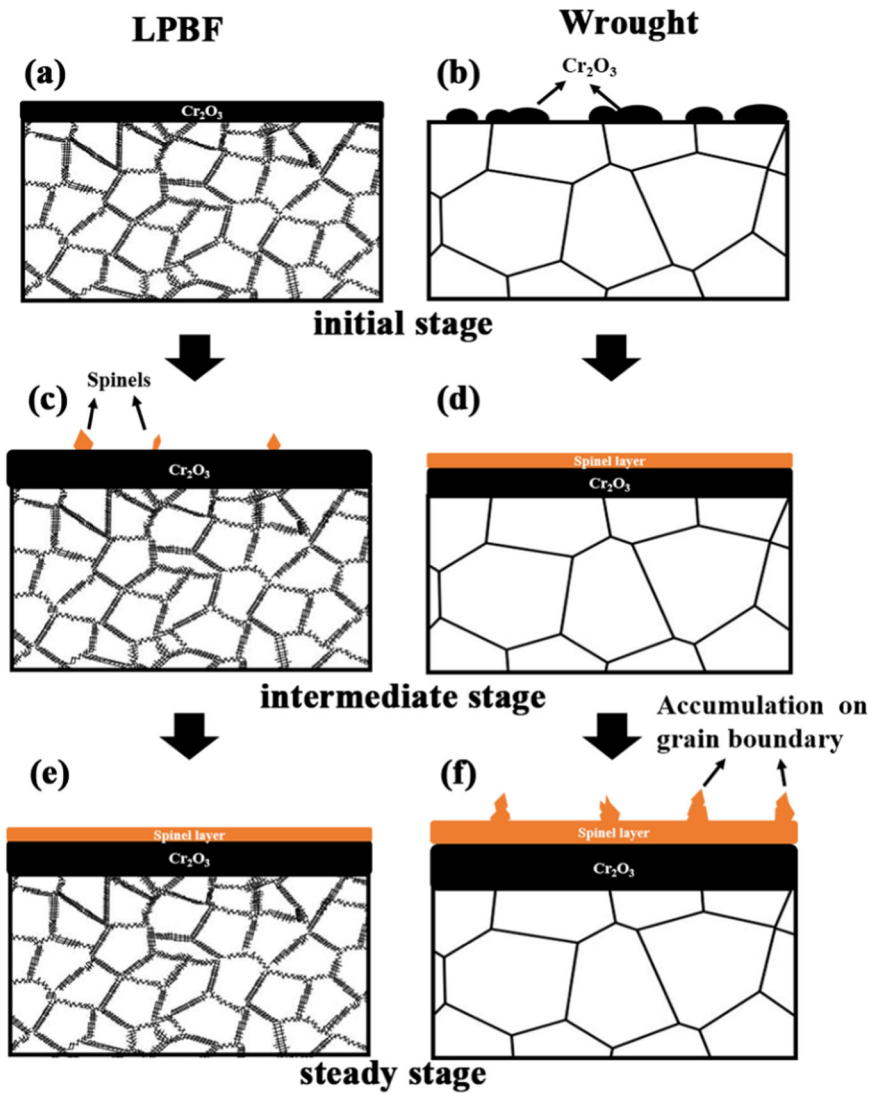
Fig. 11 Schematic diagram of oxidation behavior at different stage. a Oxidation behavior of LPBF sample at initial stage. **b** Oxidation behavior of wrought sample at initial stage. **c** Oxidation behavior of LPBF sample at intermediate stage. **d** Oxidation behavior of wrought sample at intermediate stage. **e** Oxidation behavior of LPBF sample at steady stage. **f** Oxidation behavior of wrought sample at steady stage.
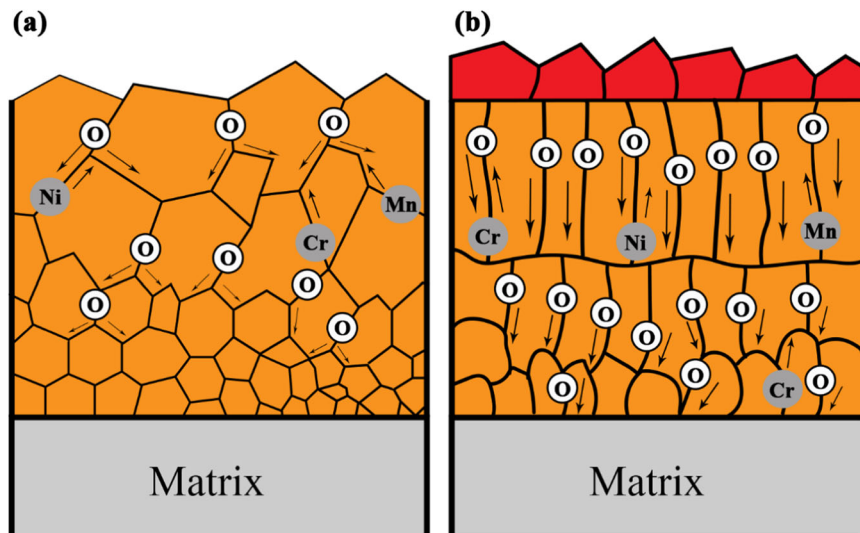

Fig. 12 Schematic diagrams of diffusion of O element in oxide film with different structure in LPBF and wrought samples. a Equiaxed structure oxide film in LPBF sample. **b** Columnar structure oxide film in wrought sample.
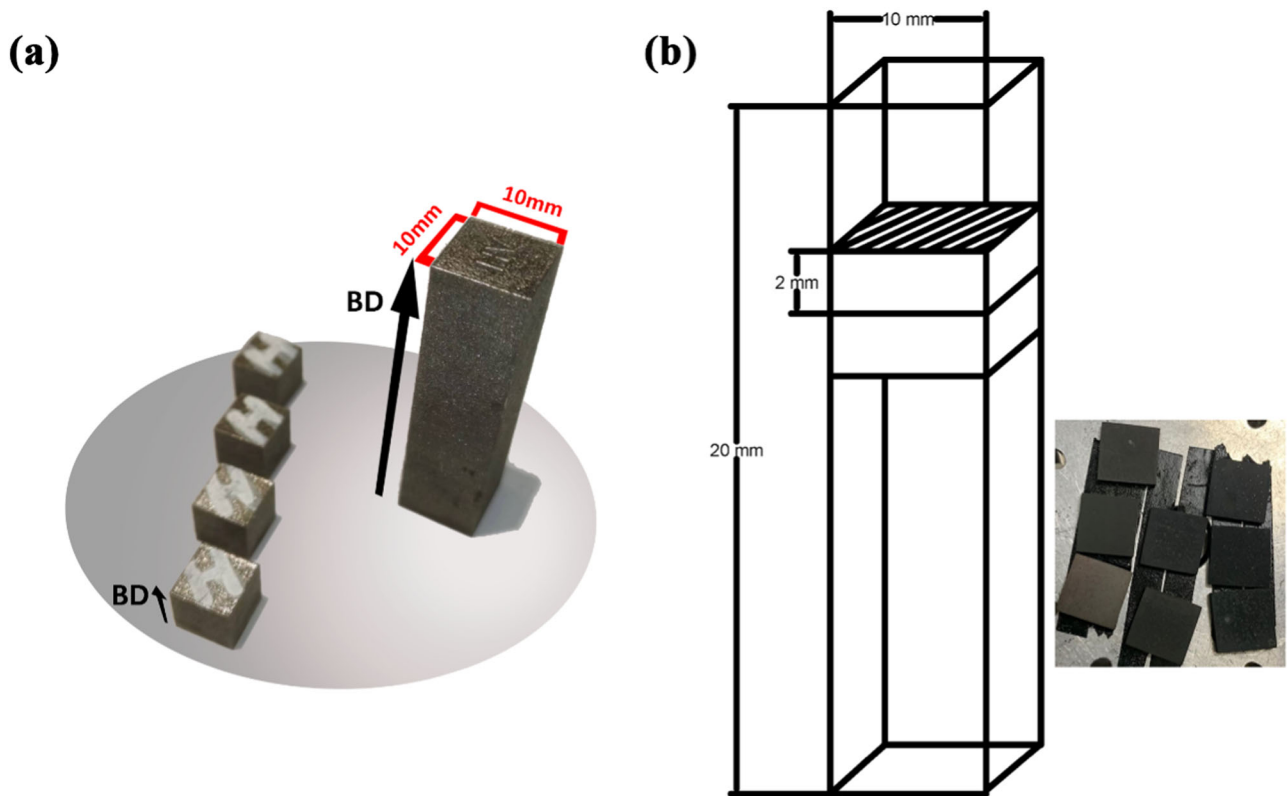
Fig. 13 Preparation and selection of oxidation experiment samples. a The raw samples for oxidation experiments. **b** Schematic diagram of samples with macrophotograph after exposure.

Table 2. Chemical composition of GH3536 powder and wrought GH3536 (wt.%).

Element	C	Cr	Co	W	Mo	Al	Ti	Ni
Powder	0.057	22.1	1.52	0.65	9.21	< 0.05	< 0.02	Bal
Wrought	0.071	21.61	1. 95	0.702	8.90	0.195	0.036	Bal
Element	Fe	B	Mn	Si	P	S	Cu	
Powder	19.0	< 0.003	< 0.05	< 0.05	< 0.005	< 0.001	< 0.02	
Wrought	17.18	< 0.010	0.660	0.142	0.009	< 0.001	< 0.50	

METHODS

Oxidized sample preparation

The pre-alloyed atomized GH3536 powder used for the LPBF process was provided by the Institute of Metal Research (IMR), Chinese Academy of Sciences, Shenyang, China. The chemical composition of the powder is summarized in Table 2. The GH3536 samples conducted in oxidation experiments were manufactured using the Ampro innovation SP100 equipped with a 200 W fiber laser. The optimized parameters used in the LPBF process contains laser power 170 W, scanning speed 1060 mm/s, hatch distance 0.08 mm and thickness 30 μm, to ensure that the density of LPBF samples was not less than 99.95%. The raw samples for oxidation experiments were produced in the form of metal cubes with the dimensions of 10 mm × 10 mm x 40 mm, as shown in Fig. 13a. The oxidation experiments for wrought GH3536 are considered as a comparison to study the difference of the microstructural characteristics of the oxide film formed on the LPBF GH3536. The chemical composition of wrought GH3536 is also displayed in Table 2.

High-temperature oxidation experiments

The LPBF GH3536 samples selected for oxidation experiments are perpendicular to the building direction (XOY plane). Prior to the oxidation experiments, the LPBF GH3536 cubes and wrought GH3536 cubes were sectioned to obtain samples with the desired dimensions for furnace exposure, 10 mm × 10 mm × 2 mm. After cutting, the six surfaces were carefully ground with SiC emery papers from 200 grit to 3000 grit and the chamfers were protected deliberately while two large faces were gradually polished with the final step being diamond paste of 1 μm, as shown in Fig. 13b. After polishing, each sample was rinsed with deionized water and then placed in an ultrasonic bath of acetone and ethanol twice for 10 min each time.

The wrought and LPBF samples were subjected to oxidation kinetics tests at 950 °C from 1 h to 500 h in air. All samples were mass weighed three times to get an average weight before exposure. After exposure, samples were cooled to room temperature and carefully extracted for examination. The oxidation tests were all conducted in a muffle furnace and the samples were placed in the same zone where the temperature deviated less than 3 °C within 5 cm. At least two parallel samples were prepared for exposure test in each condition to guarantee both the accuracy and reliability of the experimental results. The samples were weighed for three times to get an average weight again after exposing 1, 5, 10, 20, 50, 100, 200 and 500 h, respectively. The oxidation kinetics curve was obtained through the weight gains distribution with increased exposing time. To further study the microstructural characteristics of oxide film, the cross-sectional samples were carefully sliced and abraded with SiC emery paper from 1200 to 3000 grit and polished with a diamond paste spray (3, 1.5, and 0.25 μm) for following observation.

Microstructural characterization of oxide film

After 20 h exposure, the microstructure characteristics of the oxide films were selected for finer details investigation. The external oxide film characterization was carried out by means of grazing incidence X-ray diffraction (GI-XRD) conducted with a Cu–Ka source (k = 1.54 Å) in the scanning range of 20°–70° at a step size of 0.02° (Make & model: BRUKER – D8 Advance). The surface and cross-section morphology of oxide film was analyzed under SEM (Quanta FEG450) equipped with energy-dispersive spectroscopy (EDS). Element distribution and chemical composition on the cross-section of the oxide film were characterized using a Shimadzu-1720 electron probe microanalysis (EPMA).

Two cross-sectional foils samples were prepared using Focused Ion Beam (FIB) on the LPBF and wrought samples. TEM observation and transmission Kikuchi diffraction (TKD) analysis were performed on the foil samples using a FEI Tecnai G2F20 device equipped with a field emission gun operating at 200 kV and a FEI Helios G4 UX) equipped with an Oxford C-Nano EBSD detector systems that allows for better spatial resolution with minimal sample drift. The step sizes for TKD measurement were set to 10 nm. The data was subsequently post-processed by TSL OIM (version 8.0) software to obtain phase map, pole figure (PF) maps, grain boundaries (GB) maps and inverse pole figure (IPF) maps.

DATA AVAILABILITY

The authors declare that the data supporting the findings of this study are included within the paper and available from the corresponding author on reasonable request.

REFERENCES

1. Nakanishi, T. & Kawakami, H. Creep properties of Hastelloy-X in impure helium environments. *Nucl. Technol.* **66**, 273–282 (1984).
2. Kim, W. G., Yin, S. N., Ryu, W. S. & Chang, J. H. Creep properties of Hastelloy-X Alloy for the high temperature gas-cooled reactor. *Key Eng. Mater.* **326–328**, 1105–1108 (2006).
3. Aghaie-Khafri, M. & Golarzi, N. Forming behavior and workability of Hastelloy X superalloy during hot deformation. *Mater. Sci. Eng. A.* **486**, 641–647 (2008).
4. Abuzaid, W., Sehitoglu, H. & Lambros, J. Plastic strain localization and fatigue micro-crack formation in Hastelloy X. *Mater. Sci. Eng. A.* **561**, 507–519 (2013).
5. Inc. Haynes International, Hastelloy X alloy (product brochure) Information
6. Kim, W. G., Yin, S. N., Ryu, W. S., Chang, J. H. & Kim, S. J. Tension and creep design stresses of the "Hastelloy-X" alloy for high-temperature gas cooled reactors. *Mater. Sci. Eng. A* **483–484**, 495–497 (2008).
7. Pillai, R., Dryepondt, S. & Pint, B. A. High temperature oxidation lifetime modeling of thin-walled components[C]//Turbo Expo: Power for Land, Sea, and Air. *ASME* **58677**, V006T24A008 (2019).
8. Kim, W. G., Yin, S. N., Kim, Y. W. & Chang, J. H. Creep characterization of a Ni-based Hastelloy-X alloy by using theta projection method. *Eng. Fract. Mech.* **75**, 4985–4995 (2008).
9. Hayashi, S., Matsukawa, C., Yakuwa, H. & Kishikawa, T. Cyclic carburization-oxidation behavior of Hastelloy-X at 1000 ℃. *Corros. Rev.* **36**, 75–85 (2018).
10. England, D. M. & Virkar, A. V. Oxidation Kinetics of Some Nickel-Based Superalloy Foils in Humidified Hydrogen and Electronic Resistance of the Oxide Scale Formed Part II. *J. Electrochem Soc.* **148**, A330 (2001).
11. Olivares, R. I., Stein, W. & Marvig, P. Thermogravimetric study of oxidation-resistant alloys for high-temperature solar receivers. *Jom* **65**, 1660–1669 (2013).
12. England, D. M. & Virkar, A. V. Oxidation Kinetics of Some Nickel-Based Superalloy Foils and Electronic Resistance of the Oxide Scale Formed in Air Part I. *J. Electrochem. Soc.* **146**, 3196–3202 (1999).
13. Angerman, C. L. Long-term oxidation of superalloys. *Oxid. Met.* **5**, 149–167 (1972).
14. Hanbury, R. D. & Was, G. S. Oxide growth and dissolution on 316L stainless steel during irradiation in high temperature water. *Corros. Sci.* **157**, 305–311 (2019).
15. Hu, Y. B., Cheng, C. Q., Cao, T. S., Zhang, L. & Zhao, J. A study on the multiple stages of oxidation kinetics in a single crystal nickel-based superalloy. *Corros. Sci.* **188**, 1–11 (2021).
16. Yang, L., Chen, M., Wang, J., Zhu, S. & Wang, F. A duplex nanocrystalline coating for high-temperature applications on single-crystal superalloy. *Corros. Sci.* **102**, 72–83 (2016).
17. Kuang, W., Wu, X., Han, E. H. & Rao, J. The mechanism of oxide film formation on Alloy 690 in oxygenated high temperature water. *Corros. Sci.* **53**, 3853–3860 (2011).
18. Tunthawiroon, P. et al. Characterization of oxide films on wrought Co–Cr–Mo–xSi alloys exposed to high-temperature oxidation. *Corros. Sci.* **191**, 109753 (2021).
19. Min, S. et al. Influence of Defects on High-Temperature Oxidation Performance of Gh3536 Superalloys Fabricated by Laser Powder Bed Fusion, *Addit. Manuf. Lett.* **3**, 100064 (2022).
20. Min, S. et al. High-temperature oxidation performance of Ni-based GH3536 superalloy fabricated by laser powder bed fusion. *npj Mater. Degrad.* **1**, 1–12 (2022).
21. Guo, Y. et al. Improvement in the oxidation resistance of Nb-Si based alloy by selective laser melting. *Corros. Sci.* **127**, 260–269 (2017).
22. Gokcekaya, O. et al. Crystallographic orientation control of pure chromium via laser powder bed fusion and improved high temperature oxidation resistance. *Addit. Manuf.* **36**, 1–10 (2020).
23. Jia, Q. & Gu, D. Selective laser melting additive manufactured Inconel 718 superalloy parts: High-temperature oxidation property and its mechanisms. *Opt. Laser Technol.* **62**, 161–171 (2014).
24. Juillet, C., Oudriss, A., Balmain, J., Feaugas, X. & Pedraza, F. Characterization and oxidation resistance of additive manufactured and forged IN718 Ni-based superalloys. *Corros. Sci.* **142**, 266–276 (2018).
25. Romedenne, M., Pillai, R., Kirka, M. & Dryepondt, S. High temperature air oxidation behavior of Hastelloy X processed by Electron Beam Melting (EBM) and Selective Laser Melting (SLM). *Corros. Sci.* **171**, 108647 (2020).
26. Douglass, D. L. & Armijo, J. S. The effect of silicon and manganese on the oxidation mechanism of Ni-20 Cr. *Oxid. Met.* **2**, 207–231 (1970).
27. Behnamian, Y. et al. A comparative study on the oxidation of austenitic alloys 304 and 304-oxide dispersion strengthened steel in supercritical water at 650 ℃. *J. Supercrit. Fluids* **119**, 245–260 (2017).
28. Cui, C., Wu, M., He, R., Gong, Y. & Miao, X. Investigation on the columnar-to-equiaxed transition and corrosion behavior in multi-track Stellite-6 coating fabricated by laser cladding. *Mater. Chem. Phys.* **291**, 126681 (2022).
29. Peng, S., Xu, J., Jiang, S., Xie, Z. H. & Munroe, P. Unlocking the cavitation erosion-corrosion resistance of a TiCN nanocrystalline coating with an equiaxed grain structure. *Corros. Sci.* **195**, 109978 (2022).
30. Wang, F., Lou, H., Zhu, S. & Wu, W. The mechanism of scale adhesion on sputtered microcrystallized CoCrAl films. *Oxid. Met.* **45**, 39–50 (1996).

AUTHOR CONTRIBUTIONS

S.M. and H.Z. completed the experiment and the writing of the manuscript. J.H., K.Z. checked and improved the manuscript. H.L. and H.Z. assisted with the experimental work.

COMPETING INTERESTS

The authors declare no competing interests.

ADDITIONAL INFORMATION

Correspondence and requests for materials should be addressed to J. Hou.

Reprints and permission information is available at http://www.nature.com/reprints

Publisher's note Springer Nature remains neutral with regard to jurisdictional claims in published maps and institutional affiliations.